Phase separation and superparamagnetism in the martensitic phase of $Ni_{50-x}Co_xMn_{40}Sn_{10}$

S. Yuan,[1] P. L. Kuhns,[1] A. P. Reyes,[1] J. S. Brooks,[1,2,*] M. J. R. Hoch,[1,†] V. Srivastava,[3] R. D. James,[3] and C. Leighton[4]
[1]*National High Magnetic Field Laboratory, Florida State University, Tallahassee, Florida 32310, USA*
[2]*Department of Physics, Florida State University, Tallahassee, Florida 32310, USA*
[3]*Department of Aerospace Engineering and Mechanics, University of Minnesota, Minneapolis, Minnesota 55455, USA*
[4]*Department of Chemical Engineering and Materials Science, University of Minnesota, Minneapolis, Minnesota 55455, USA*
(Received 11 December 2015; revised manuscript received 25 February 2016; published 21 March 2016)

$Ni_{50-x}Co_xMn_{40}Sn_{10}$ shape memory alloys in the approximate range $5 \leqslant x \leqslant 8$ display desirable properties for applications as well as intriguing magnetism. These off-stoichiometric Heusler alloys undergo a martensitic phase transformation at a temperature T_M of 300–400 K, from ferromagnetic (FM) to nonferromagnetic, with unusually low thermal hysteresis and a large change in magnetization. The low temperature magnetic structures in the martensitic phase of such alloys, which are distinctly inhomogeneous, are of great interest but are not well understood. Our present use of spin echo nuclear magnetic resonance in the large hyperfine fields at ^{55}Mn sites provides compelling evidence that nanoscale magnetic phase separation into FM and antiferromagnetic (AFM) regions occurs below T_M in alloys with x in the range 0 to 7. At finite Co substitution, the FM regions are found to be of two distinct types, corresponding to high and low local concentrations of Co on Ni sites. Estimates of the size distributions of both the FM and AFM nanoregions have been made. At $x = 7$, the AFM component is not long-range ordered, even below 4 K, and is quite different from the AFM component found at $x = 0$; by $x = 14$, the FM phase is completely dominant. Of particular interest, we find for $x = 7$ that field cooling leads to dramatic changes in the AFM regions. These findings provide insight into the origins of magnetic phase separation and superparamagnetism in these complex alloys, particularly their intrinsic exchange bias, which is of considerable current interest.

DOI: 10.1103/PhysRevB.93.094425

I. INTRODUCTION

Magnetic shape memory alloys of the type Ni-Mn-X (where X = Sn, In, Ga, etc.) have been the subject of intense recent investigation due to their technological importance and their rich variety of structural, mechanical, magnetic, and thermodynamic properties. Often these alloys undergo a martensitic phase transformation at or above room temperature, with great potential for applications in the areas of sensors, actuators, magnetic refrigeration, etc. [1–9]. Much of the recent research has focused on off-stoichiometric versions of the full Heusler alloys, of the form $Ni_{50}Mn_{25+y}X_{25-y}$, in which competing ferromagnetic (FM) and antiferromagnetic (AFM) interactions between Mn atoms on inequivalent sites give rise to tunable magnetic phase competition. The competing interactions lead to the emergence of unanticipated magnetic behavior, including superparamagnetism (SP) in bulk samples and intrinsic exchange bias (EB) effects [10–12].

Important recent developments involve quaternary systems such as Ni-Co-Mn-X [13–18], especially around the composition $Ni_{50-x}Co_xMn_{40}Sn_{10}$ [14–18]. Interest in these Co-substituted alloys, particularly those with $5 \leqslant x \leqslant 8$, is linked to the low thermal hysteresis associated with the martensitic transformation at temperature T_M. The transition from FM order above T_M to a state without long-range FM order below T_M is accompanied by a large change in magnetization [3,16]. Low thermal hysteresis at the transition is an indication of an invariant lattice plane at martensite-austenite interfaces at temperatures near T_M [19,20]. This condition applies, to a good approximation, in $Ni_{50-x}Co_xMn_{40}Sn_{10}$ for a limited range of x [16–18]. These alloys then exhibit desirable properties for applications, including a high Curie temperature, and a martensitic transition from an FM phase to a low magnetization non-FM phase at T_M above ambient (340 K for $x = 6$).

A magnetic phase diagram has recently been proposed for $Ni_{50-x}Co_xMn_{40}Sn_{10}$, with three distinct regions, designated I ($0 \leqslant x \leqslant 4.5$), II ($4.5 < x \leqslant 11$), and III ($x > 11$) [18]. In this phase diagram, similar to an earlier one [21], the valence electron per atom ratio, e/a, decreases with x, and there is an accompanying decrease in T_M from 420 K at $x = 0$ to around 300 K at $x = 10$ [18], dropping to 0 K for $x \geqslant 11$. We focus primarily on Region II here, where on cooling, ferromagnetism appears in the austenite (at T_Cs of 425–450 K), followed by a martensitic transition to a much lower magnetization non-FM state. As in Region I, SP then emerges but at lower temperatures, ~50 K. The blocking temperature, T_B, exhibits a marked and largely unexplained change near $x = 4.5$, i.e., at the transition between Regions I and II. In Region III, the FM austenite phase persists to low T with no martensitic transformation. Notably, the EB blocking temperature, T_{EB}, below which intrinsic EB effects are detected, is distinct from T_B in Region I but coincident with T_B in Region II.

Recent small-angle neutron scattering (SANS) experiments on polycrystalline $Ni_{50-x}Co_xMn_{40}Sn_{10}$ ($x = 6$ and 8) show that the SP and EB effects are linked to a magnetically inhomogeneous low temperature state. The results provide strong evidence of nanoscale magnetic phase separation in this material, with a liquidlike spatial distribution of SP clusters in a non-FM matrix [17]. While AFM order and paramagnetism in the non-FM matrix could not be distinguished, various indirect observations pointed to some form of AFM order [17,18]. The magnetization behavior with temperature provided additional

*Deceased
†Corresponding author: hoch@magnet.fsu.edu

evidence for clusters and, in the case of $x = 6$, gives $T_B \approx 60$ K [17]. The SANS, together with magnetization, provided information on the FM cluster sizes and separations. The detailed natures of the FM clusters remain unclear, however, as do the characteristics of the matrix.

Our recent paper using ^{55}Mn nuclear magnetic resonance (NMR) on $Ni_{50}Mn_{40}Sn_{10}$ (i.e., $x = 0$), sheds further light on these issues by investigating the SP at this composition and, critically, by elucidating the nature of the non-FM matrix phase [22]. The latter was shown to indeed be AFM, as opposed to being simply paramagnetic, but with short- rather than long-range magnetic order. In essence, both FM and AFM clusters occur, with both a distribution in sizes and distinct temperature dependences. In the present paper, we again apply low temperature ^{55}Mn NMR, this time studying polycrystalline $Ni_{50-x}Co_xMn_{40}Sn_{10}$ across all three interesting magnetic regions, specifically at $x = 7$ (in the martensitic phase) and $x = 14$ (in the austenite phase), for comparison with our previous findings for $x = 0$. The ^{55}Mn hyperfine-field-NMR results provide detailed information on the ground state magnetic properties as a function of x and on the evolution of the inhomogeneous nanoscale magnetic structures with temperature. At $x = 7$, two distinct FM regions and a dominant AFM region are detected at low temperatures, with the FM regions having very different characters (identified with high and low local concentrations of Co) and the AFM regions being highly thermally unstable. This is quite different from $x = 0$, reflecting the increase in stability of the FM phase with Co substitution, confirmed by our measurements at $x = 14$. Information obtained on the size distribution of the nanoscale FM and AFM clusters, together with their proximity and temperature dependent dynamics, helps to elucidate the origins of the macroscopic magnetic properties represented in the phase diagram of these alloys. In particular, radical changes in AFM regions are evidenced with field cooling (FC) at $x = 7$, directly relevant to the intrinsic EB phenomena that have attracted such attention in these and related systems.

II. EXPERIMENTAL RESULTS

Polycrystalline samples of $Ni_{50-x}Co_xMn_{40}Sn_{10}$ with selected x (0, 7, and 14) were prepared by arc melting high purity metal starting materials under argon followed by annealing at 900 °C for 24 hours before quenching in water [16–18]. The ingots were then powdered and annealed to provide samples for NMR (with suitable radio frequency [RF] penetration), as described previously [22]. Characterization was carried out using energy dispersive spectroscopy, differential scanning calorimetry, x-ray diffraction, and magnetometry. Experiments on the $x = 0$ sample are described in our prior paper [22]. At $x = 7$, the transition temperatures are $T_M = 370$ K and $T_C = 430$ K, with low thermal hysteresis at the martensitic transition, $\Delta T_M \sim 6$ K. The $x = 14$ sample has $T_C = 460$ K and does not undergo a martensitic transformation.

The ^{55}Mn (gyromagnetic ratio $\gamma/2\pi = 10.5$ MHz T^{-1}) NMR measurements presented here were made mainly in zero applied magnetic field but also in fields $\mu_0 H$ up to 6 T using a spin echo spectrometer with automated frequency sweep capability over the range $f = 150$–450 MHz. The

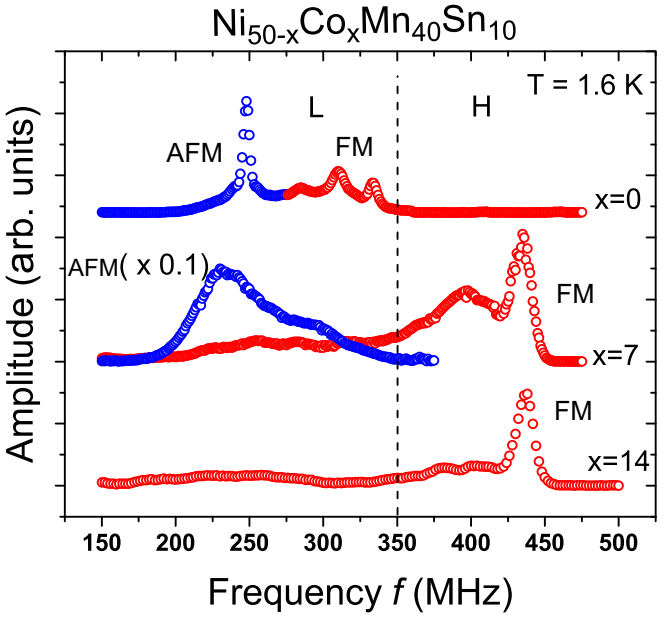

FIG. 1. Frequency (f) scanned ^{55}Mn zero applied field NMR spectra in polycrystalline $Ni_{50-x}Co_xMn_{40}Sn_{10}$ at 1.6 K for $x = 0$, 7, and 14. Spectra associated with ferromagnetic regions (FM, red) and antiferromagnetic regions (AFM, blue) are indicated. The amplitude of the dominant AFM component has been reduced by a factor 10 in the $x = 7$ spectrum. Comparison of the spectra reveals that substitution of Co on Ni sites at $x = 7$ and 14 produces ferromagnetic regions or clusters with enhanced hyperfine fields and spectral features above 350 MHz, compared to $x = 0$. The spectra can be well fit using multiple Gaussian curves. The spectral region below 350 MHz is designated L (low frequency) and the region above 350 MHz is designated H (high frequency), as discussed in the text.

polycrystalline metallic grains were embedded in paraffin wax to minimize skin depth effects. Zero-field (ZF) spectra were observed in the hyperfine fields experienced by ^{55}Mn nuclei, which ranged from ~20 to 43 T, and were recorded as a function of temperature (T) by increasing the frequency in 1 MHz steps over the required range. As described in Ref. [22], the magnetic system NMR signal enhancement factor, η, which is given by $\eta = B_{\rm hf}/B_{\rm A}$, where $B_{\rm hf}$ is the hyperfine field and $B_{\rm A}$ is the anisotropy field, can effectively distinguish FM and AFM regions since η is typically significantly larger in FM regions than in AFM regions. As discussed in our prior paper [22], further confirmation of the FM/AFM assignments is provided by measurements of spectral frequency shifts in low (~1 T) applied magnetic fields; lines attributable to the FM component downshift with H, in contrast to the behavior of spectral lines from AFM regions.

Low temperature (1.6 K), zero-field-cooled (ZFC) NMR spectra, recorded at optimal RF power levels in each case and obtained by integrating the spin echo signals at stepped frequencies, are shown in Fig. 1 for $x = 0$, 7, and 14. The $x = 0$ spectrum has previously been discussed [22] and is shown for comparison with the $x = 7$ and $x = 14$ spectra. On this plot, the open circle (blue) data are associated with low η (~10) spectral components from ^{55}Mn sites in regions of the sample that have AFM character and are labeled AFM. In contrast, the open circle (red) data are due to FM regions, with

$\eta \sim 225$, and are labeled FM. Comparison of the spectra shows that substitution of Co on a fraction of the Ni sites leads to major changes in the spectral features. In particular, the $x = 7$ and $x = 14$ spectra have FM components at $f > 350$ MHz, designated Region H in the figure (high frequency), that are not present for $x = 0$. In addition, for $x = 7$ the spectral features below 350 MHz, designated Region L in the figure (low frequency), involve broad AFM and FM components, with the AFM of dominant importance only at the lowest temperatures ($T < 5$ K, see below). Note that for $x = 7$, the amplitude of the large AFM component has been reduced by a factor of 10.The area of a particular peak in the ^{55}Mn spectrum is proportional to the number of Mn atoms that contribute to that peak. A comparison of the spectral areas, with allowance for differences in the enhancement factors, thus provides an estimate of the volume fractions of the FM and AFM regions. The necessity of a scaling factor for the $x = 7$ AFM in Fig. 1 is due to the dominant importance of this component. Examination of the spectral areas at this x value shows that at 1.6 K the AFM constitutes ~90% of the magnetic material in this sample, as discussed in greater detail in Sec. III.A. For $x = 14$ on the other hand, no AFM signals are observed over the entire frequency range, but there are distinct FM features in Region H and a broad weak response in Region L. These changes in the spectra induced by the substitution of Co on some of the Ni sites are discussed in full in Sec. III, but we note immediately that they clearly reflect radical changes in the magnetic properties.

As the temperature is raised, the forms of the FM spectral features for $x = 7$ and $x = 14$ do not change significantly, but the amplitudes steadily decrease and the 1.6 K spectral peaks in Region H gradually shift to lower frequencies. Figure 2 illustrates the latter point by showing the T dependence of the frequency ratio f/f_0 for the principal FM spectral component for $x = 7$, taking $f_0 = 435$ MHz at 1.6 K. Over the range 1.6 to 150 K, f decreases from 435 MHz to 405 MHz. Qualitatively similar shifts are found over this T range for the FM component at $f_0 \sim 400$ MHz (see Fig. 1). Notably, the frequency ratio versus T plot in Fig. 2 shows a marked decrease in f/f_0 as T increases from 1.6 to 5 K (inset), followed by a more gradual linear decrease from 5 to 70 K. For $T > 70$ K, the ratio f/f_0 decreases rapidly again, and the NMR signal amplitude diminishes to zero. The approximately linear T dependence (solid black fit line) suggests a mechanism involving dynamics of the FM clusters, as discussed below and established in our prior paper [22].

In order to also analyze the evolution of the spectral weight with temperature, the peaks for the $x = 7$ and $x = 14$ samples were fit with multiple Gaussian curves (not shown). For $x = 7$, the behavior of the Curie-law-corrected area of the FM components in Region H is plotted (in arbitrary units) as a function of T in Fig. 3. This spectral area is proportional to the number of ^{55}Mn nuclei, which experience hyperfine fields that are effectively *static* on the NMR timescale (~10μs) and which can therefore contribute to the observed spin echo signals [22]. The temperature scaling compensates for the Curie law decrease in the nuclear magnetization. For SP clusters of volume V, the NMR blocking temperature, $T_B^{NMR}(V)$, is the temperature above which NMR signals from these clusters can no longer be detected [22]. If there

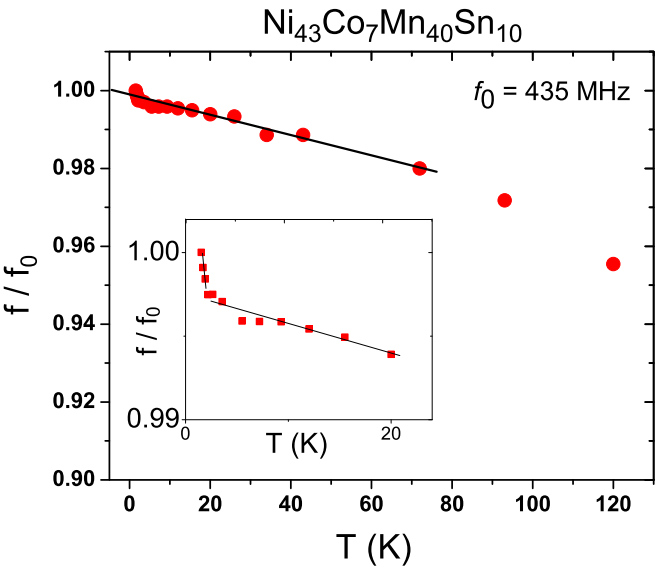

FIG. 2. The ratio, f/f_0, of the ^{55}Mn NMR resonance peak center frequency (f) to the resonance frequency (f_0) at 1.6 K, as a function of T, for the principal FM component in Region H (i.e., the highest frequency in Fig. 1) for $Ni_{43}Co_7Mn_{40}Sn_{10}$. The frequency decreases approximately linearly at temperatures in the range 3–70 K and then more rapidly at higher temperatures. The decrease in frequency is produced by averaging of the hyperfine field by collective cluster spin fluctuations in their anisotropy fields. The slope of the straight line fit through the points provides an estimate of the average cluster size, as discussed in the text. The small reproducible increase in f/f_0 at the lowest temperatures (<3 K), as shown in the inset, is attributed to the freezing of very small clusters and a possible change in the spectral lineshape.

is a distribution of cluster sizes, it follows that there is a corresponding distribution of T_B^{NMR} values.

It can be seen from Fig. 3 that the T-scaled integrated area (in arbitrary units) of the FM component at $x = 7$ plateaus at low T but exhibits a gradual fall-off with increasing T, up to 300 K. The FM spectral area versus T plot in Fig. 3 is fit (solid red line) using the SP cluster model we previously established [22] with a distribution of FM cluster sizes (inset), as described further in Sec. III. In marked contrast, the dashed line in Fig. 3 shows the rapid decrease in the T-corrected areas of the AFM component in Region L (again in arbitrary units to facilitate a comparison with the behavior of the relatively small FM component). The AFM shows no plateau down to 1.6 K, very different to the $x = 0$ case in Ref. [22]. The rapid decrease in amplitude of the Region L broad AFM component with increasing T, until it is no longer observable at $T > 10$ K, evidences a marked decrease in thermal stability of the AFM regions in comparison to the AFM at $x = 0$. It should be noted, however, that at $x = 7$ the broad low frequency FM component (in Region L) is still observable, albeit with reduced amplitude, above 100 K. At low T (<4 K), and in low H, this FM component is masked by the dominant AF and emerges in the spectra only above 10 K.

Figure 4 highlights a different aspect of the data. Specifically, Fig. 4(a) shows the T dependence of the $x = 7$ spin-lattice relaxation time T_1 for the principal high frequency FM

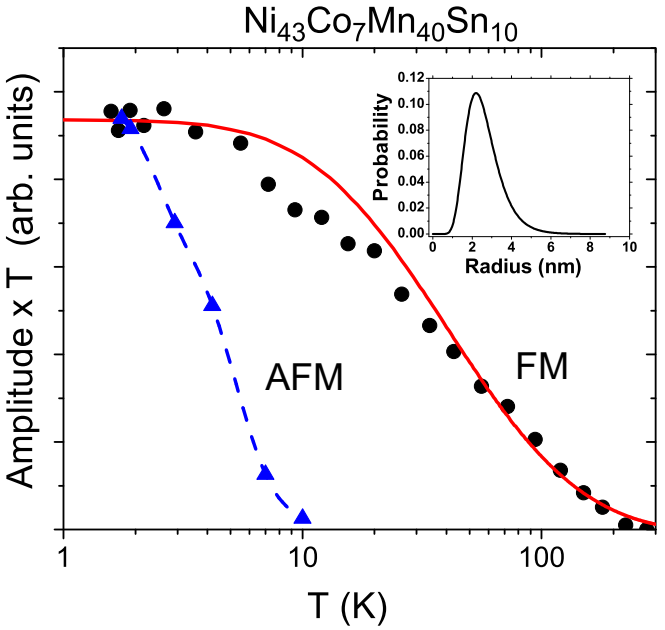

FIG. 3. Curie-law-corrected ^{55}Mn NMR peak areas for the high frequency (region H in Fig. 1) ferromagnetic components (black circles) in $Ni_{43}Co_7Mn_{40}Sn_{10}$ as a function of temperature. The fitted curve is based on a cluster dynamics model, with a distribution of cluster sizes, as described in the text. The inset shows the log-normal cluster radius distribution used in the fit; assuming spherical clusters, the most probable diameter is 4.4 nm. For comparison the Curie-law-corrected areas for the AFM component (region L in Fig. 1) are also shown (blue triangles). This AFM component cannot be detected at $T > 10$ K.

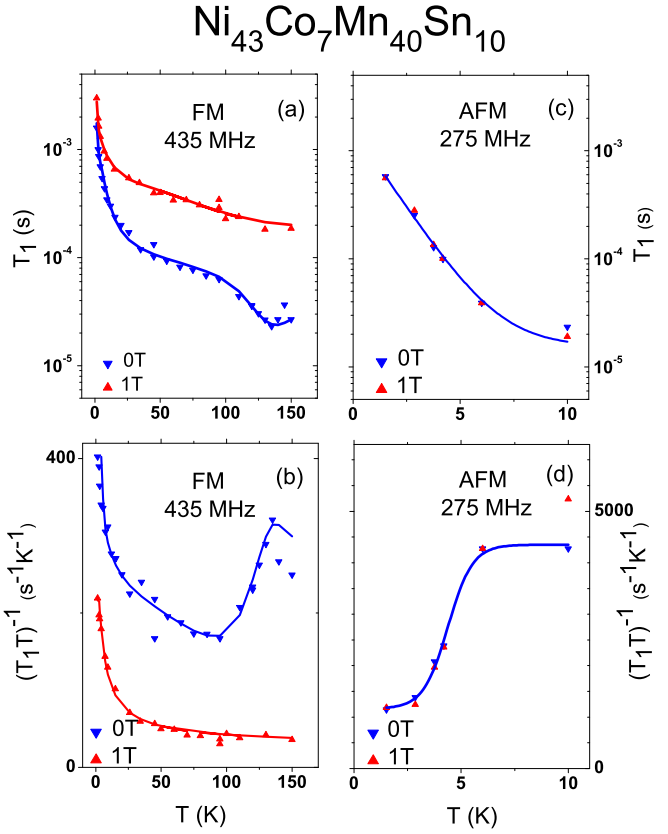

FIG. 4. ^{55}Mn spin-lattice relaxation times T_1 for (a) the principal FM spectral component in Region H and (c) the AFM components in Region L (see Fig. 1) as a function of temperature in $Ni_{43}Co_7Mn_{40}Sn_{10}$. Measurements were made in both zero field and in an applied field of 1 T. Comparison of the FM and AFM T_1 values shows that the AFM relaxation times are substantially shorter than those of the FM component and that they decrease more rapidly as T increases. The field dependence seen in Fig. 4(a) is discussed in the text. (b), (d) Korringa plots of $1/T_1T$ versus T for the FM and AFM components, respectively. An estimate of the density of states at the Fermi level for the FM components is given in the text.

component, while Fig. 4(c) gives the behavior of T_1 for the AFM component in Region L. Measurements were made in ZF and in 1 T. Figures 4(b) and 4(d) then show the corresponding Korringa plots of $1/T_1T$ versus T for the FM (Region H) and AFM (Region L) components, respectively. These dynamic data are discussed in full in Sec. III.

Finally, the transverse or spin-spin relaxation time T_2, obtained from stretched exponential fits to the spin echo decay curves at $x = 7$, is found to be weakly T dependent and, for the FM components in Region H, decreases from 110 μs to <10 μs as T increases from 1.6 K to 120 K. Figure 3 shows that the *spectral area* decreases steadily over this same temperature range, as the regions in which $T_2 < 10$ μs no longer contribute significantly to spin echoes. T_1 in the FM regions is roughly an order of magnitude longer than the corresponding T_2.

III. DISCUSSION

The principal findings of the present paper may be summarized as follows. Substitution of Co for Ni in $Ni_{50-x}Co_xMn_{40}Sn_{10}$ leads to dramatic changes in the low temperature ^{55}Mn ZF spectra for $x = 7$ and $x = 14$, in comparison with the $x = 0$ spectrum, as can be seen in Fig. 1. Among other differences, new FM components appear above 350 MHz. This major change in the form of the spectra with x suggests that Co substitution for Ni produces significant changes in the local electronic structure, generating enhanced hyperfine fields at ^{55}Mn sites in the vicinity of the Co ions. In addition, at $x = 7$ the broad FM and AFM spectral components in Region L, centered at about 275 MHz and 230 MHz, respectively, occur at frequencies similar to those of the spectral features at $x = 0$. However, the narrow FM and AFM components seen near 300 and 250 MHz for $x = 0$ [22] are *not* seen at $x = 7$. In our prior paper on $x = 0$ [22], these features were interpreted as originating from the largest FM and AFM clusters in the sample. The $x = 7$ FM and AFM spectral lines in Region L are attributed to Mn in regions that have comparatively low Co concentrations and correspondingly little change in the ^{55}Mn hyperfine field compared to $x = 0$. Below, we provide further discussion of specific aspects of the data.

Fluctuations in local Co concentrations, which give rise to Co-rich and Co-poor regions in the $x = 7$ and $x = 14$ alloys, may be due, at least in part, to natural statistical fluctuations similar to those that produce the nanoscale phase separation found in the cobaltite oxides, for example [23]. It is also possible that in the Ni-Co-Mn-Sn alloys, the cluster formation is driven by free energy modifications linked to changes in

the local electronic and magnetic structure induced by the replacement of Ni by Co. Recent ferromagnetic resonance and x-ray magnetic circular dichroism (XMCD) experiments on $Ni_{45}Mn_{36.7}In_{13}Co_{5.1}$, made over a temperature range that includes both the austenite and martensite phases, have shown that substitution of Co for Ni enhances FM exchange and weakens AFM correlations in this alloy. Mixed AFM and FM regions are found to coexist below 50 K [24]. Additionally, x-ray absorption spectroscopy (XAS) and XMCD measurements made on epitaxial films of $Ni_{48}Co_5Mn_{35}In_{12}$, in which Co is substituted on both Ni and Mn sites, reveal significant changes in the magnetic interactions in this Heusler alloy at temperatures both above and below T_M [25]. The present NMR experiments provide evidence for nanoscale FM and AFM clusters in $Ni_{50-x}Co_xMn_{40}Sn_{10}$ alloys but do not shed obvious light on the mechanism that produces the clusters.

A. NMR spectral amplitude changes with temperature

The Curie law (T-scaled) corrected spectral areas (proportional to the number of ^{55}Mn nuclei in regions that contribute to the corresponding NMR signals) steadily decrease with T, consistent with a distribution of cluster sizes, and a corresponding distribution of $T_B^{NMR}(V)$ values [22]. Most notably, the area of the 230 MHz AFM component decreases dramatically in the range 1.6–10 K, as shown in Fig. 3 for $x = 7$, evidencing thermal instability of these regions with low T_B^{NMR} characteristics. In contrast, the T-scaled area of the broad low amplitude FM spectral component in Region L decreases gradually with rising T from 1.6–150 K, similar to that of the 435 MHz component shown in Fig. 3. This behavior points to broad distributions of the FM cluster sizes and associated NMR blocking temperatures in both Regions L and H.

The spectral area results, considered together, suggest that the largest FM and AFM ordered regions, responsible for the narrow spectral features found below 350 MHz for $x = 0$ [22], have their long range correlated spin structures distinctly altered by the incorporation of Co on Ni sites in the $x = 7$ and $x = 14$ cases. This important finding indicates that the abrupt decrease in the dc magnetization SP blocking temperature, T_B, from ~120 K to 70 K, at around $x = 4.5$ in the phase diagram [18], i.e., the Region I/Region II boundary, which has proven difficult to understand, is a result of a reduction in the size of SP clusters produced by the substitution of Co on a critical fraction of Ni sites. Furthermore, it is possible that local austenite-like regions are produced at sufficiently large Co concentrations. While these arguments, in general, agree with prior statements on decreasing thermal stability of the FM clusters in Region II of the phase diagram compared to Region I (consistent with the reduced T_B) [18], this new understanding highlights changes in the cluster size *distribution* (i.e., elimination of the largest clusters), which was not explicitly considered earlier [18]. As mentioned above, the substitution of Co for Ni results in a large change in B_{hf} at ^{55}Mn sites, indicating that the local electronic structure is considerably modified by the Co substitution. While it is possible that there is a transfer of spin density to Mn produced by the replacement of Ni by Co, this is likely to be a small effect as the bulk of the spin density is already concentrated on the Mn in the Ni_2MnSn system [26]. The local crystal structure in a particular region is likely to depend on the Co concentration and the geometrical configuration of Co on neighboring Ni sites. Variations in this local structure could produce the multiple components seen in Fig. 1 for $x = 7$ and 14, together with the observed increase in linewidth as f decreases. It is also interesting to note the similarity in the high frequency, Region H, spectral lineshapes in the $x = 7$ and $x = 14$ alloys. This similarity supports the suggestion that for $x = 7$, the austenite phase is stabilized at low temperatures in regions with high Co concentrations.

In order to quantitatively compare the relative concentrations of Mn in the various magnetic regions of the present samples, it is necessary to take into account variations in the RF enhancement factor, η, which was used in Sec. II to distinguish the AFM and FM components in the $x = 7$ ^{55}Mn spectra. Using the values for η given in Sec. II, together with the relationship $\eta = B_{hf}/B_A$, yields $B_A = 0.19$ T for the anisotropy field of the FM component in Region H for $x = 7$, with a similar value for $x = 14$. This value for the anisotropy field is similar to that found for the FM components in $Ni_{50}Mn_{40}Sn_{10}$ [22]. From the relative areas of the ^{55}Mn spectra, which are shown with proper allowance for the difference in η values, it is then possible to obtain the ratio of the numbers of FM and AFM Mn atoms, denoted N_{FM} and N_{AFM}, respectively. For $x = 7$ at 1.6 K, we obtain $N_{FM}/N_{AFM} = 0.1$, meaning that the AFM component is of dominant importance, producing ~90% of the combined FM plus AFM NMR signal. This is in contrast to the $x = 0$ case, in which $N_{FM}/N_{AFM} \approx 0.8$, i.e., close to unity [22]. The major part of the FM constituent (~75%) for $x = 7$ is in Region H.

The substitution of a fraction of the Ni by Co leads to major changes in the nanoscale magnetic structure of these systems. In a comparison of the NMR results obtained for $x = 0$ and $x = 7$, it is the disappearance of *spatially extended* AFM regions for $x = 7$, as revealed by their low T_B^{NMR} values (<10 K), as inferred from Fig. 3, which is particularly striking. In addition, the NMR-detected FM regions at $x = 7$ are separated into the low and high frequency components, in Regions L and H, respectively, and, as discussed above, are, at 1.6 K, greatly diminished in relative intensity compared to AFM. These findings suggest that in regions of these alloys, the exchange interactions between Mn atoms are significantly altered through the replacement of some Ni by Co. Note as an aside that the NMR results suggest that a fraction of the smallest FM and AFM clusters are not detected, even at temperatures as low as 1.6 K, due to cluster dynamics.

B. Cluster size estimates

In order to quantify the cluster sizes, especially for the FM regions generating the SP behavior, analysis of the data shown in Fig. 2 is useful. In particular, the SP globular cluster model described in Ref. [22] predicts that for a FM cluster of volume V at temperatures below $T_B^{NMR}(V)$, the slope of an f/f_0 versus T plot is given by $k_B/(2K_AV)$, where K_A is the anisotropy energy density. For a system in which there is a distribution of cluster sizes, the analysis is less straightforward. In order to obtain a rough estimate of the average cluster size, however, we assume that the cluster model can be applied to the $f_0 = 435$ MHz component frequency dependence on T (Fig. 2). We take $K_A = \frac{1}{2}n\mu B_A$, where $\mu = 4\mu_B$, n is the

spin density, and $B_A = 0.19$ T, as given above. (We assume that K_A is the same for all of the FM clusters, but we cannot exclude the possibility of some distribution of K_A values linked to cluster sizes and shapes.) From the slope of the straight line fit through the points in the range 3–70 K in Fig. 2, we obtain an average cluster diameter $D \sim 9$ nm. It should be noted here that because of the distribution of cluster sizes, with a corresponding distribution of $T_B^{NMR}(V)$ values, there is a gradual decrease in signal amplitude with T (see Fig. 3) as the smaller clusters pass through their respective blocking temperatures. It therefore follows that this size estimate (9 nm) is somewhat skewed towards the larger clusters. The inset to Fig. 2 shows that at the very lowest T (1.6–3 K) the slope of the f-T curve increases, consistent with a growth in proportion of small volume clusters, accompanied by an upward frequency shift. The size estimate of 9 nm from the slope in Fig. 2 is somewhat larger than the previously reported value of 2–6 nm for $x = 6$ [17], a point that will be returned to below. As a final comment on the analysis of Fig. 2, we note that above 70 K the frequency variation is no longer linear in T, and the simple form given by the cluster model no longer applies.

It is possible to obtain further information on the size distribution of the FM clusters in Region H, which, based on the 1.6 K spectral areas, make up ~7% of the total NMR detected magnetic material (with AFM ~90% and total FM ~10%) in the $x = 7$ sample at low T by using our SP cluster model to fit the Curie-law-corrected area plot in Fig. 3. The procedure is described in Ref. [22] and involves the use of the following expression for the nuclear spin-spin relaxation rate for a globular cluster of volume V

$$\frac{1}{T_2} = \tfrac{1}{12} S(S+1)\left(\frac{\omega_I^2}{\omega_S^2}\right)\left(\frac{T}{T^*}\right)^2\left(\frac{1}{\tau_c}\right), \qquad (1)$$

where $\omega_I = 2\pi f_{hf}, \omega_S = 2\pi/\tau_0$ with τ_0 the pre-exponential factor in the Néel-Arrhenius (N-A) expression, and $T^* = K_A V/k_B$. The correlation time,τ_c, is determined by the coupling of a cluster spin to the lattice and can, in principle, be modeled using a modified form of the N-A relation with the anisotropy energy reduced by a significant factor. For clusters of volume V with the minimum observable $T_2 \sim 10\,\mu$s, we find that $\tau_c \to \tau_0$ as $T \to T_B^{NMR}(V)$. For a system in which there is a distribution of SP cluster volumes, described by a probability distribution $P(V)$, there is a corresponding distribution of T_2 [22]. The amplitude of the NMR signal will then decrease as T is raised and fewer clusters contribute to the signal as their T_2 values fall below the NMR measurement time $\tau_m = 10\,\mu$s. Making use of the Poisson distribution, the model predicts that the NMR spin echo signals from clusters of a particular size should decay as $S(T) = S_0 \exp(-\tau_m/T_2)$, where $S(T)$ is the signal amplitude at temperature T and S_0 is the signal amplitude from these clusters at the lowest T. Using Eq. (1) and integrating numerically over a log-normal volume distribution provides the reasonable fit to the FM spectral area plot, shown in Fig. 3. The size distribution of the FM clusters obtained from the fit is shown in the inset to Fig. 3, the most probable diameter being $D \sim 4.4$ nm. We emphasize that while the fitting process does involve a number of adjustable parameters, the size distribution is found to be fairly robust to changes in these parameters. However, the integration over cluster volumes using a broad size distribution may be an oversimplification of the actual situation. Comparison of the sizes obtained from the two approaches we have used, based on Figs. 2 and 3, respectively, which differ by a factor 2, suggests that the average cluster diameter lies in the range 3–10 nm, with the most probable diameter ~6 nm. Notably, this range overlaps the estimate of 2–6 nm made previously for $x = 6$ [17]. Note that the line for the AFM spectral area curve in Fig. 3, over the limited range 1.6–10 K, is simply a guide to the eye rather than a fit. The nature and size of the AFM regions is unclear, but the NMR evidence suggests numerous small regions with $D \sim 1$ nm but which are probably not globular in shape.

While the spheroidal cluster model approach used in the analysis of the NMR results is certainly an idealization of the magnetic substructures in $Ni_{50-x}Co_xMn_{40}Sn_{10}$, the cluster size estimates thus obtained are consistent with the SANS and magnetometry estimates [18]. The microscopic picture of the $x = 7$ alloy that is provided by the ^{55}Mn NMR results is summarized as follows: There are two different types of FM regions, corresponding to Co-rich and Co-poor clusters, respectively. These FM regions have a distribution of nanoscale sizes, and, in addition, there is an AFM component that is of dominant importance in the system at temperatures below 10 K. Above 10 K, the AFM region cannot be detected by spin echo NMR due to collective spin dynamic effects that shorten the transverse (spin-spin) nuclear relaxation times. The FM components associated with Co rich and Co poor regions are detected up to 150 K, but both signals show a marked decrease in amplitude with rising temperature as a result of a cluster size distribution in the range 3–10 nm. At $x = 14$, no AFM is detected, while two FM components are found with the Region H response from Co-rich regions being of dominant importance.

C. Connections to EB effects

Having elucidated the x dependence of the low T spectra shown in Fig. 1 and having quantitatively analyzed the behavior shown in Figs. 2 and 3 to extract volume fractions of the coexisting AFM and FM phases, relative thermal stabilities, and cluster sizes, we now turn specifically to the EB effects that have gathered such attention in these and related materials. As mentioned in Sec. I, EB effects are detected in dc magnetization measurements on $x = 7$ samples, for instance, at $T < T_B \sim 50$ K. For EB to occur in a simple picture, it is necessary that interactions between spins at FM-AFM interfaces provide a pinning mechanism for the FM spins [27–30]. In experiments involving layered magnetic films, it has been shown (e.g., Refs. [30] and [31]) that uncompensated spins in the AFM play a crucial role in establishing EB effects.

In order to investigate the EB in detail, we carried out FC experiments on the $x = 7$ alloy. Figure 5(a) shows the Region L AFM spectral component, centered at 240 MHz, in ZF following FC to 1.7 K with fields in the range $0 \leqslant \mu_0 H \leqslant 6$ T. Surprisingly, striking changes in the amplitude of the AFM component are produced by FC. The 255 MHz FM component in Region L is not detectably changed by FC for $\mu_0 H \leqslant 0.15$ T, while at higher fields the behavior of this component is masked by the large growth in amplitude of the AFM component. On the other hand, the FM components in Region H, which comprise ~70% of the total FM regions,

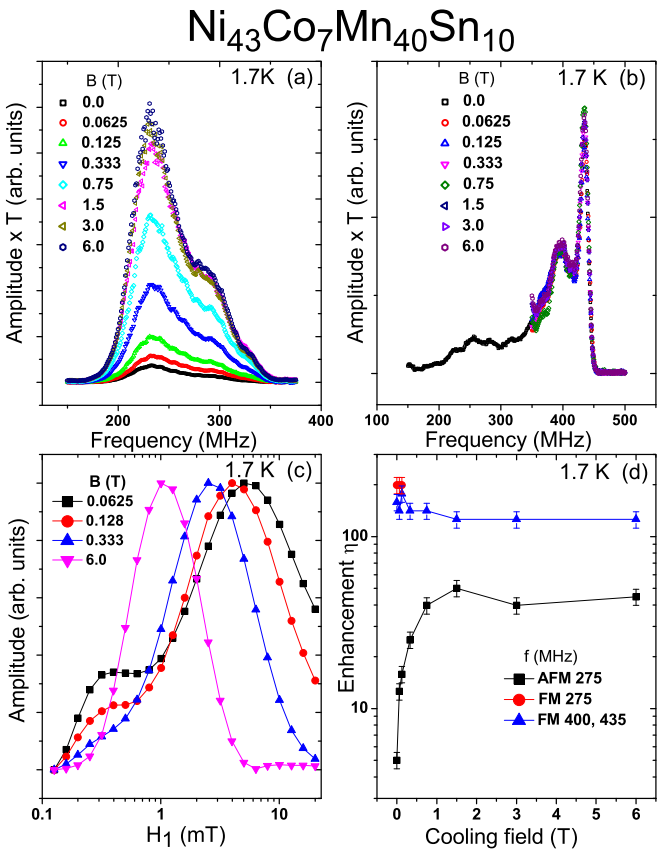

FIG. 5. (a) ^{55}Mn zero field spectra in the range 150–375 MHz, obtained in various RF fields, H_1, optimized for the 240 MHz AFM component, following field cooling to 1.7 K in varied applied fields up to 6 T. (b) ^{55}Mn zero field spectra, obtained in a fixed low RF field optimized for the 435 MHz component, over the range 150–500 MHz, following field cooling to 1.7 K in fields up to 6 T. (c) Spin echo amplitude response curves at 275 MHz and 1.7 K, obtained in zero field as a function of H_1, following field cooling in fields up to 6 T. The marked *decrease* in the optimal H_1 with increase in the $\mu_0 H$ used during field cooling is due to an unexpected large increase in the enhancement factor η, as discussed in the text. (d) Plot of η versus $\mu_0 H$ following field cooling to 1.7 K, as obtained from Fig. 5(c). The dramatic increase in η is attributed to exchange bias linked interactions between the FM and AFM regions across their interfaces.

are unchanged in FC-ZF-run experiments, as can be seen in Fig. 5(b). The FC response of the AFM and FM components at this x value are thus starkly different. The increase in AFM spectral amplitude is in part attributed to alignment of spins along H (perpendicular to the RF field), which is the optimal orientation for NMR but more significantly is due to an order of magnitude *increase* in η, as shown in Fig. 5(d). This figure panel shows η as a function of the cooling field for the AFM/Region L, FM/Region L, and FM/Region H components, emphasizing that only the AFM is strongly influenced by FC. These η values are derived from Fig. 5(c), which shows 1.7 K plots of the ZF spin echo amplitudes, obtained at 275 MHz following FC in fields up to 6 T, recorded as a function of the amplitude of the RF field H_1 for a *fixed* RF pulse length. It is clear that following FC the optimal H_1 shifts to lower values, corresponding to an increase in η. Note that for $f = 275$ MHz at low $\mu_0 H$ (<0.1 T), there are two distinct maxima in the spin echo response curves, corresponding to the high H_1, low η, AFM components, and the low H_1, high η, FM components, respectively. As noted above, for $f = 240$ MHz, the FM component is less well resolved, and the AFM is of dominant importance. As $\mu_0 H$ is increased, the difference in the η values for the AFM and FM components decreases, as seen in Figs. 5(c) and 5(d). Interestingly, in FC experiments for $x = 0$, the observed changes in the signal amplitude and in η are much smaller than in $x = 7$, where the AFM and FM cluster sizes are reduced in size. The enhanced detection of EB-linked effects by NMR for $x = 7$ compared to $x = 0$ is clearly facilitated by modifications in the nanoscale geometry of spin clusters induced by the insertion of Co for Ni.

Based on these observations it is possible to reach the following conclusions on EB in the $x = 7$ system. First, the dominant FM components in Region H, which are associated with high Co concentrations and modified local crystal structures, appear to play, at best, a minor role in the EB process, while the interactions between the FM and AFM components in Region L are of dominant importance in producing the effect. Second, exchange interactions at the AFM-FM interfaces in Region L produce an increase in the η values for the AFM of more than an order of magnitude. These η values approach those of the FM regions to within a factor $\sim$3. This novel and interesting finding concerning the coupling of spins and their linked dynamics at the FM-AFM interface in $x = 7$ complements previous EB experiments involving magnetization measurements on $Ni_{44}Co_6Mn_{40}Sn_{10}$ [17,18]. In addition, the change in the nanoscale cluster properties of the AFM component between $x = 0$ and $x = 7$ provides a basis for explaining the distinct change in T_{EB} at $x \sim 4.5$ in the phase diagram given in Ref. [18].

As the temperature is raised towards 10 K, the role of the AFM component, as detected by NMR, diminishes in importance (Fig. 3). The dc magnetization measurements show that for $4.5 \leqslant x \leqslant 10$ EB effects are no longer observable above 50 K, which is also the dc SP blocking temperature. The significant difference in T_{EB} from NMR ($\sim$10 K) and dc measurements (50 K) reflects the different response times of these techniques to collective spin dynamics. Differences between NMR T_B^{NMR} and dc T_B values are, as with EB effects, attributed to the different dynamic processes detected by the two types of measurements, as discussed in Ref. [22]. In sum, these low temperature experiments show that for $x = 7$ the AFM/Region L spin clusters or layers, seen below 10 K in Fig. 3, are of dominant importance in providing the EB interfacial pinning mechanism for the FM/Region L spins. The NMR thus provides compelling evidence that the shift in the dc $M - \mu_0 H$ loop due to EB is primarily due to interactions at the AFM-FM interfaces in Region L associated with the low Co martensitic components. In addition, interactions between FM spins in Regions L and H are likely to play some role in the EB process.

D. Spin-lattice relaxation and cluster dynamics

Turning now to further analysis of dynamic data, we note that the T_1 versus T plots for the high frequency FM component

in ZF and in 1 T, as shown in Fig. 4(a) for $x = 7$, reveal an initial marked decrease below 20 K, followed by a more gradual decrease at higher T. For the AFM component, T_1 decreases rapidly with increasing T, over the range 1.6–10 K, consistent with thermally induced small cluster spin flips that give rise to fluctuating local fields responsible for spin-lattice relaxation. The most dynamic small clusters do not contribute to the spin echo signals since $T_B^{NMR} < 1.6$ K for these clusters. They can, of course, play a role in inducing relaxation in their larger neighbors, which are observed by NMR.

We have not attempted a quantitative analysis of the AFM relaxation behavior shown in Figs. 4(c) and 4(d) and concentrate on the FM component T_1 in Region H over the range 1.6–150 K, as presented in Figs. 4(a) and 4(b). In order to explain the behavior of T_1 with T in Fig. 4(a), two competing relaxation mechanisms need to be considered. First, intercluster dynamic dipolar interactions, involving the small cluster spin flips, and second, the intracluster Korringa mechanism involving conduction electron scattering. The relative importance of these mechanisms is dependent on the cluster size, and it is instructive to consider the Korringa-style plot of $1/T_1T$ versus T in Fig. 4(b). The large decrease in $1/T_1T$ produced by a field of 1 T points to field suppression of the fluctuating intercluster dipolar mechanism through alignment of cluster moments parallel to H and a reduction in the transverse fluctuating field because of partial cancellation of fields from various neighbor clusters. The Korringa plateau value for $T > 20$ K in Fig. 4(b) then allows us to estimate the density of states at the Fermi level in the larger FM clusters using the Moriya expression $\frac{1}{T_1^K} = C\langle\frac{1}{r_A^3}\rangle_{FM}(\rho_\uparrow^2 + \rho_\downarrow^2)F(\Gamma)$, where $C = (16\pi/5)\mu_0^2\gamma_I^2\mu_B^2\hbar k_B T$, μ_B is the Bohr magneton, γ_I is the nuclear gyromagnetic ratio, and $\rho_\uparrow$ and $\rho_\downarrow$ are the densities of states (DOS) at the Fermi energy, E_F, for spin up and spin down electrons, respectively [32]. The inverse radius cubed, averaged over the Fermi surface, is $\langle 1/r_A^3\rangle_F = 0.32 \times 10^{32}$ m^{-3} [22]. The function $F(\Gamma)$ gives the t_{2g} orbital admixture in the wave function at E_F. If we take $F(\Gamma) = 1$ as an approximation in estimating the DOS at the Fermi energy, we obtain $(\rho_\uparrow^2 + \rho_\downarrow^2) = 0.8$ eV f.u.$^{-1}$, which is roughly half the value obtained for the DOS in FM regions of $Ni_{50}Mn_{40}Sn_{10}$ [22]. Substitution of Ni by Co leads to this large decrease in the Fermi level DOS for the 435 MHz FM component (Region H) in the $x = 7$ alloy.

IV. CONCLUSIONS

Our hyperfine-field-mediated NMR measurements provide considerable nanoscale information on the magnetic nature of the shape memory alloys $Ni_{50-x}Co_xMn_{40}Sn_{10}$ with $x = 0$, 7, and 14. In both finite x alloys, the incorporation of Co on a fraction of the Ni sites leads to the formation of new types of FM nanoregions, or clusters, with distinct NMR features when compared to $x = 0$. In the case of $x = 14$ at low temperatures, the spectral signatures of two FM regions are identified (although one is dominant), and it is suggested that these regions correspond to high and low local Co concentrations. For $x = 7$, at temperatures well below the martensitic transition, there are also two FM regions, again linked to high and low Co, this time coexisting with an AFM region. Both of the FM regions have broad size distributions, as revealed by spectral area versus temperature plots over the range 1.6–200 K. The results have been interpreted in terms of a distribution of NMR blocking temperatures in each case. The similar mixed magnetic phase behavior found for both $x = 7$ and $x = 14$ suggests that local structural variations persist to low temperatures in these systems, possibly linked to the coexistence of small austenite and martensite regions. Signals from the AFM regions, which play the key role in establishing intrinsic EB effects in the $x = 7$ system, are observed in NMR spin echo experiments only at temperatures below 10 K. This thermally unstable AFM component, which may be viewed as a matrix in which the FM regions are embedded, is of dominant importance in terms of volume fraction at temperature below 5 K. These regions provide a dynamically correlated environment for the FM clusters as the temperature is raised. The FC experiments show that it is the low Co concentration FM regions that couple to the AFM component to establish EB. Direct evidence for this interaction is obtained from changes in NMR signal enhancement.

ACKNOWLEDGMENTS

The work at the National High Magnetic Field Laboratory was supported by National Science Foundation (NSF) DMR-1157490 and by the State of Florida. JSB received funding from NSF-DMR 1309146. Work at the University of Minnesota (UMN) in CL's group was supported by the Department of Energy under Award No. DE-FG02-06ER46275. Work at UMN in RDJ's group was supported by the Air Force Office of Scientific Research-Multidisciplinary University Research Initiative under Grant No. FA9550-12-1-0458, the NSF Partnerships for International Research and Education under Grant No. OISE-0967140, and by the Office of Naval Research under Grant No. N00014-14-1-07141. The assistance of Daniel Phelan with sample fabrication is gratefully acknowledged.

[1] *Magnetism and Structure in Functional Materials*, edited by A. Planes, L. Mañosa, and A. Saxena, Vol. 79 (Springer, New York, 2005).

[2] T. Krenke, E. Duman, M. Acet, E. F. Wassermann, X. Moya, L. Mañosa, and A. Planes, Nat. Mater. **4**, 450 (2005).

[3] T. Krenke, M. Acet, E. F. Wassermann, X. Moya, L. Manosa, and A. Planes, Phys. Rev. B **72**, 014412 (2005).

[4] T. Krenke, M. Acet, E. F. Wassermann, X. Moya, L. Manosa, and A. Planes, Phys. Rev. B **73**, 174413 (2006).

[5] Y. Sutou, Y. Imano, N. Koeda, T. Omori, R. Kainuma, and K. Ishida, Appl. Phys. Lett. **85**, 4358 (2004).

[6] M. Khan, I. Dubenko, S. Stadler, and N. Ali, J. Phys. Condens. Matter, **20**, 235204 (2008).

[7] P. Entel, M. Stewart, M. E. Gruner, H. C. Herper, D. Comtesse, R. Arroyave, N. Singh, A. Talapatra, V. V. Sokolovsky,

V. D. Buchelnikov, F. Albertini, L. Righi, and V. A. Cherenko, Eur. Phys. J. B. **86**, 65 (2013).
[8] S. Aksoy, M. Acet, P. P. Deen, L. Mañosa, and A. Planes, Phys. Rev. B **79**, 212401 (2009).
[9] M. Ye, A. Kimura, Y. Miura, M. Shirai, Y. T. Cui, K. Shimada, H. Namatame, M. Taniguchi, S. Ueda, K. Kobayashi, R. Kainuma, T. Shishido, K. Fukushima, and T. Kanomata, Phys. Rev. Lett. **104**, 176401 (2010).
[10] Z. Li, C. Jing, J. Chen, S. Yuan, S. Cao, and J. Zhang, Appl. Phys. Lett. **91**, 112505 (2007).
[11] M. Khan, I. Dubenko, S. Stadler, and N. Ali, Appl. Phys. Lett. **91**, 072510 (2007).
[12] B. M. Wang, Y. Liu, P. Ren, B. Xia, K. B. Ruan, J. B. Yi, J. Ding, X. G. Li, and L. Wang, Phys. Rev. Lett. **106**, 077203 (2011).
[13] R. Kainuma, Y. Imano, W. Ito, Y. Sutou, H. Morito, S. Okamoto, O. Kitakami, K. Oikawa, A. Fujita, T. Kanomata, and K. Ishida, Nature **439**, 957 (2006).
[14] D. Y. Cong, S. Roth, J. Liu, Q. Luo, M. Pötschke, C. Hürrich, and L. Schultz, Appl. Phys. Lett. **96**, 112504 (2010).
[15] D. Y. Cong, S. Roth, M. Pötschke, C. Hürrich, and L. Schultz, Appl. Phys. Lett. **97**, 021908 (2010).
[16] V. Srivastava, X. Chen, and R. D. James, Appl. Phys. Lett. **97**, 014101 (2010).
[17] K. P. Bhatti, S. El-Khatib, V. Srivastava, R. D. James, and C. Leighton, Phys. Rev. B **85**, 134450 (2012).
[18] K. P. Bhatti, V. Srivastava, D. P. Phelan, S. El-Khatib, R. D. James, and C. Leighton in *Heusler Alloys*, edited by A. Hirohata and C. Felser (Springer, Berlin, 2015).
[19] J. Cui, Y. S. Chu, O. O. Pomodu, Y. Furuya, J. Hattrick-Simpers, R. D. James, S. Thienhang, M. Wuttig, Z. Zhang, and I. Takeuchi, Nat. Mater. **5**, 286 (2006).
[20] V. Srivastava, X. Chen, and R. D. James, Acta Mater. **57**, 4332 (2009).
[21] D. Y. Cong, S. Roth, and L. Schultz, Acta. Mater. **60**, 5335 (2012).
[22] S. Yuan, P. L. Kuhns, A. P. Reyes, J. S. Brooks, M. J. R. Hoch, V. Srivastava, R. D. James, S. El-Khatib, and C. Leighton, Phys. Rev. B **91**, 214421 (2015).
[23] C. He, S. El-Khatib, J. Wu, J. W. Lynn, H. Zheng, J. F. Mitchell, and C. Leighton, Europhys. Lett. **87**, 27006 (2009).
[24] K. Ollefs, C. Schöppner, I. Titov, R. Meckenstock, F. Wilhelm, A. Rogalev, J. Liu, O. Gutfleisch, M. Farle, H. Wende, and M. Acet, Phys. Rev. B **92**, 224429 (2015).
[25] P. Klaer, H. C. Herper, P. Entel, R. Niemann, L. Schultz, S. Fähler, and H. J. Elmers, Phys. Rev. B **88**, 174414 (2013).
[26] S. Ishida, Y. Kubo, J. Ishida, and S. Asano, J. Phys. Soc. Japan, **48**, 814 (1980).
[27] W. H. Meiklejohn and C. P. Bean, Phys. Rev. **105**, 904 (1957).
[28] Ch. Binek, A. Hochstrat, and W. Kleemann, J. Magn. Magn. Mat. **234**, 353 (2001).
[29] H. Ohldag, A. Scholl, F. Nolting, E. Arenholz, S. Maat, A. T. Young, M. Carey, and J. Stöhr, Phys. Rev. Lett. **91**, 017203 (2003).
[30] S. Roy, M. R. Fitzsimmons, S. Park, M. Dorn, O. Petracic, I. V. Roshchin, Z.-P. Li, X. Batlle, R. Morales, A. Misra, X. Zhang, K. Chesnel, J. B. Kortright, S. K. Sinha, and I. K. Schuller, Phys. Rev. Lett. **95**, 047201 (2005).
[31] X. Zhou, L. Ma, Z. Shi, W. J. Fan, R. F. Evans, J-G. Zheng, R. W. Chantrell, S. Mahngin, H. W. Zhang, and S. M. Zhou, Scientific Reports **5**, 9183 (2015).
[32] T. Moriya, J. Phys. Soc. Japan **19**, 681 (1964).